AGU PUBLICATIONS

JGR

Journal of Geophysical Research: Atmospheres

RESEARCH ARTICLE
10.1002/2015JD024370

**Key Points:**
- Geological changes in the Cenozoic have changed summertime climate in Asia
- The continental-scale structure of the summer monsoon circulation remains robust
- Large local climate changes occur, with insolation and local topography having the largest impacts

**Correspondence to:**
G. H. Roe,
gerard@ess.washington.edu

**Citation:**
Roe, G. H., Q. Ding, D. S. Battisti, P. Molnar, M. K. Clark, and C. N. Garzione (2016), A modeling study of the response of Asian summertime climate to the largest geologic forcings of the past 50 Ma, *J. Geophys. Res. Atmos.*, *121*, doi:10.1002/2015JD024370.

Received 20 OCT 2015
Accepted 2 APR 2016
Accepted article online 9 APR 2016



# A modeling study of the response of Asian summertime climate to the largest geologic forcings of the past 50 Ma

**Gerard H. Roe[1], Qinghua Ding[2], David S. Battisti[2], Peter Molnar[3], Marin K. Clark[4], and Carmala N. Garzione[5]**

[1]Department of Earth Space Sciences, University of Washington, Seattle, Washington, USA, [2]Department of Atmospheric Sciences, University of Washington, Seattle, Washington, USA, [3]Department Geological Sciences, University of Colorado Boulder, Boulder, Colorado, USA, [4]Department Earth Environmental Sciences, University of Michigan, Ann Arbor, Michigan, USA, [5]Department Earth Environmental Sciences, University of Rochester, Rochester, New York, USA

**Abstract** The modern Asian summer monsoon is known to be affected by the modern continental geometry, orography, atmospheric composition, interglacial climate state, and orbital configuration. All of these factors, however, have undergone substantial changes since the Indian and Asian continents collided 50 million years ago. Within the framework of one general circulation model we evaluate the relative importance of each of these factors for the spatial patterns of summertime climate fields and precipitation-weighted $^{18}O$. We find that the continental-scale structure of the monsoon circulation remains robust, but there are important impacts on local environmental conditions. The largest differences in climate are associated with changes in orbital configuration and topography because of how those factors influence local gradients in the summer climate variables. Finally, model calculations are consistent with the modern understanding of monsoon dynamics in which the strength of the circulation and the distribution of rainfall are tightly coupled to the spatial patterns of low-level moist static energy and upper tropospheric temperature.

## 1. Introduction

Since the collision of the Indian and Asian continents around fifty million years ago (50 Ma), there have been large changes in the factors that govern Asia's climate. Relative plate motions include more than 2000 km of convergence between central Asia and India [e.g., *Molnar and Stock*, 2009], resulting in a rearrangement of land-ocean geometry in the Indian Ocean and also in the growth of high terrain that includes the Tibetan Plateau and adjoining mountain ranges. In conjunction with these movements, reconfigurations of inland seas [e.g., *Popov et al.*, 2004] have altered the moisture balance and the thermal inertia and albedo of the surface. Atmospheric carbon dioxide, although still uncertain, has perhaps been as high as 1500 ppmv and as low as about 200 ppmv [e.g., *Zhang et al.*, 2013]. The onset and subsequent fluctuations of the Pleistocence ice ages entailed extensive changes in Northern Hemisphere ice cover and topography. Moreover, throughout this interval, the climate has been subject to the quasiperiodic oscillations of Earth's orbital parameters that have redistributed solar radiation as a function of season and latitude. Each of these factors has the potential to influence climate in ways that paleoclimate observations could potentially detect.

The researcher who reconstructs paleo-environments of Asia also often aims to attribute a climatic cause. However, not only are the states of these various factors uncertain at any past time but also because these factors act in combination, an attribution to a unique factor may not be possible. Rather than aggregating all of these factors into a single attempt at a simulation [e.g., *Ramstein et al.*, 1997], our approach here is to impose stylized representations of each factor into a general circulation model (GCM). For each factor, we want to understand the resulting differences in climate and their relative importances. We restrict our analyses to summertime precipitation and temperature, and annual-mean precipitation-weighted $\delta^{18}O$, which are the climate fields most commonly reconstructed from paleoclimate proxies.

## 2. The Climate Model and Its Modern Climatology

We employ the European Centre/Hamburg (ECHAM)4.6 atmospheric general circulation model [*Roeckner et al.*, 1996] with a module for water isotopes. The model is run at T42 (about 2.8°) resolution and is coupled to

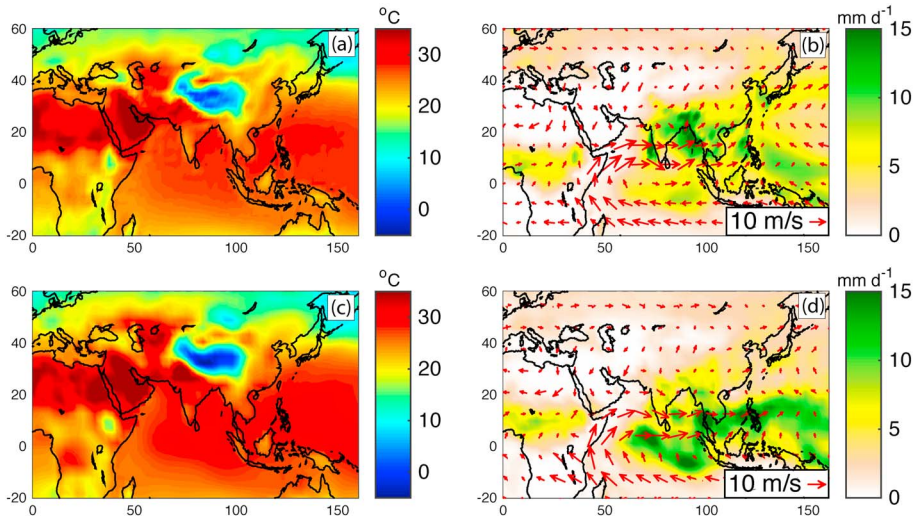


**Figure 1.** (a) Observed June to August (JJA) near-surface air temperature; (b) observed precipitation (colors) and 850 mbar winds; (c, d) same as Figures 1a and 1b, respectively, but for the ECHAM model control climate. Temperature and wind observations are from NCEP/NCAR reanalysis [*Kalnay et al.*, 1996]. Precipitation observations are from the Global Precipitation Climatology product [*Adler et al.*, 2003].

a 50 m slab ocean. It has a simple thermodynamic sea ice scheme, fixed land surface parameters (vegetation, soil permeability, etc.), and ocean water isotopes that are specified at Standard Mean Ocean Water. The isotope module includes evaporative, liquid, and ice fractionation and retains information about isotopes in the land surface scheme [*Hoffmann and Heinmann*, 1997; *Hoffmann et al.*, 1998; *Werner et al.*, 2011]. A limited set of runs were performed at higher resolution (T106, or ~1.1°) but were found to produce no significant differences from the lower resolution analyses, except where noted. A seasonally varying heat flux (or "*q* flux") is added to the slab ocean to account for ocean heat transport and errors in the model's surface energy balance. These *q* fluxes ensure that the model's modern climatology reproduces observed modern sea surface temperatures (SSTs) and sea ice extent. The same *q* fluxes are included in all our runs, but SSTs and sea ice are free to adjust to the imposed climate forcing. The SST differences in our experiments do not, however, reflect the differences in *q* fluxes that would accompany any differences in ocean circulation. The use of *q* fluxes is a compromise that allows for computational efficiency and is consistent with our idealized approach, described below, of changing one factor at a time. All of the runs were for at least 40 years, with output from the last 30 years used to construct climatologies and climatological differences. Unless explicitly noted, all results presented are significant at 95% confidence or higher, based on a two-sided *t* test [e.g., *vonStorch and Zwiers*, 1999].

The model is first run with modern boundary conditions: 360 ppmv $CO_2$ and modern insolation, continental geometry, orography, and ice sheets (Figure 2a). We define summertime here as June to August (≡JJA). The model's modern climatology reproduces the broad patterns of the observed JJA temperatures, precipitation, and low-level (850 mbar) winds (Figure 1). There are some biases: ECHAM JJA temperatures are slightly too warm over land by about a degree (cf. Figures 1a and 1c); observed JJA precipitation over the Bay of Bengal maximizes farther to the north and west in observations than in ECHAM, consistent with southwesterly low-level mean winds in observations and more westerly low-level mean winds in ECHAM. Other precipitation maxima are generally collocated in observations and ECHAM but with different relative magnitudes. A precipitation maximum along the southern front of the Himalayas is found in observations but not in ECHAM (cf. Figures 1b and 1d). This orographically induced maximum does appear in higher-resolution ECHAM runs, reported in *Battisti et al.* [2014]. However, we found that using lower resolution does not affect the differences between pairs of model runs that are our main focus here.

Overall, the level of (dis)agreement between Figures 1a and 1b is fairly typical among the current generation of GCMs. ECHAM scores approximately in the middle of the current suite of GCMs for monsoon

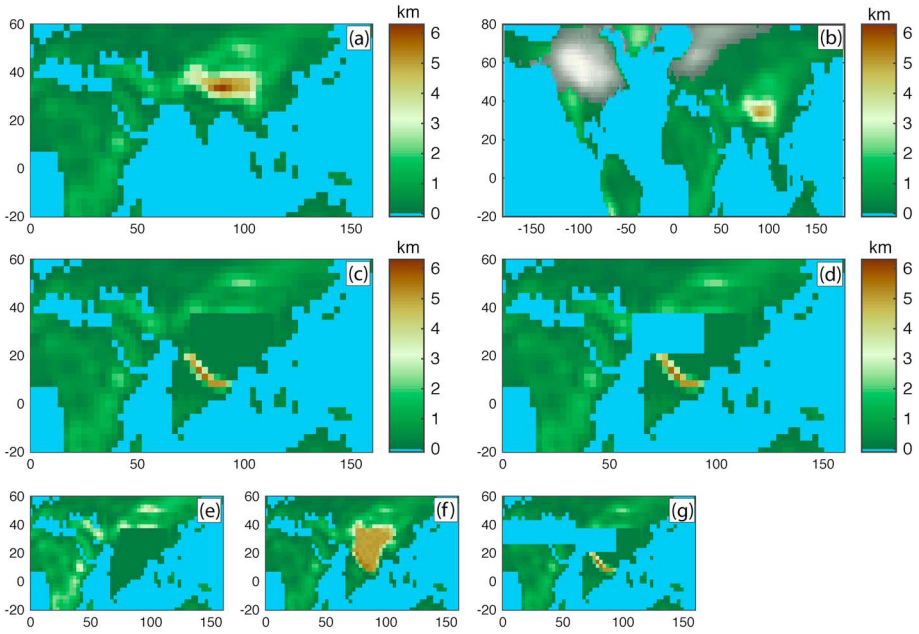


**Figure 2.** Surface topography for the various experiments shown at model resolution. (a) Control: modern topography; (b) LGM boundary conditions: LGM ice sheets plus sea level differences (shown on an expanded domain); (c) Himalaya South: stylized Indian geometry for ~50 Ma, retaining topography of the modern Himalaya; (d) Paratethys: same as Himalaya South but with a stylized Paratethys Sea added; (e) Flat South: coastline as in Himalaya South but Himalaya removed; (f) Mega-Tibet: coastline as in Himalaya South but interior plateau retained; (g) Greater Paratethys, as in Figure 2d but with Paratethys extending to the Atlantic.

metrics [e.g., *Sperber et al.*, 2013]. It is worth bearing in mind that models rarely replicate magnitudes of localized precipitation maxima within uncertainties. In the vicinity of such maxima, even a small fractional change can show up as a large absolute precipitation change, so one should be careful to not overinterpret such differences in the model runs.

A variety of geologic materials (e.g., soils, cave stalagmites, fossilized teeth, etc.) have been analyzed to recover the $\delta^{18}$O of the water they incorporated during their formation. For some of these materials, and in particular, for stalagmites, the time for formation and the mixing of the relevant waters means that variations in the $\delta^{18}$O can be interpreted as proxies for variations in the annual-mean, precipitation-weighted $\delta^{18}$O of the precipitation ($\equiv \overline{\delta^{18}O_P}$). Of course this interpretation requires an additional assumption that there are no significant changes in the fractionation processes during the formation of the proxy record. Also, it is important to note that some carbonate materials (e.g., soils) subsample the seasonal cycle in precipitation and so likely do not reflect annual-mean conditions.

If $P(t)$ and $\delta^{18}O(t)$ are the annual cycles in precipitation and oxygen isotopes, we can write

$$\overline{\delta^{18}O_P} = \frac{\int P(t)\delta^{18}O(t)dt}{\int P(t)dt}, \tag{1}$$

where the integral is taken over the annual cycle. Differences in $\overline{\delta^{18}O_P}$ are thus weighted by the seasonal cycle in precipitation and so are predominantly associated with summertime differences throughout Asia [*Dayem et al.*, 2010; *Battisti et al.*, 2014].

## 3. Five Idealized Experiments

We compare the impact of each of five separate factors that have influenced Asia's climate over the last 50 Ma. Obviously, these are not intended as simulations of an actual climate state. Rather, they are stylized experiments to evaluate the pattern and magnitude of the climate response to each factor in turn. Our approach

matches that of *Prell and Kutzbach* [1992], who analyzed a similar set of idealized experiments inspired by late Miocene and Pliocene conditions. The five factors are as follows:

1. *Orbital configuration.* We evaluate the difference in climate caused by the insolation differences between 218 kyr B.P. (thousand of years before present) and 207 kyr B.P. The 218 kyr B.P. is a time of high summertime insolation in the northern subtropics: throughout much of the subtropics, insolation differences during JJA exceed 70 W $m^{-2}$, compared to 207 kyr B.P. [e.g., *Battisti et al.*, 2014]. The difference in summertime insolation between 218 kyr B.P. and 207 kyr B.P. is the largest in northern subtropics during the last 1 Myr. All other factors are held at their modern levels. Summertime insolation at 207 kyr B.P. differs from the modern by less than 10 W $m^{-2}$ and so can be loosely identified with modern JJA conditions. *Battisti et al.* [2014] discussed this pair of runs in some detail.
2. *Atmospheric carbon dioxide.* We evaluate the difference in climate caused by raising $CO_2$ levels from 360 ppmv to 720 ppmv, a doubling. Although the data are uncertain, some reconstructions would allow for a larger range of $CO_2$ concentrations over the past 50 Ma. Low values, of approximately 180 ppmv during glaciations, are well constrained from ice cores. At the high end, values possibly exceeded 1440 ppmv in the early Eocene [e.g., *Pagani et al.*, 2011; *Zhang et al.*, 2013], although the various estimates range widely and are, in places, mutually inconsistent [e.g., *Masson-Delmotte et al.*, 2013]. Our choice for these experiments represents a substantial climate forcing, without giving undue emphasis to the highly uncertain upper bounds. Given the approximately base two logarithmic dependence of radiative forcing on $CO_2$ concentrations [e.g., *Myhre et al.*, 1998], our specific model results can be extrapolated to other $CO_2$ values (but see *Caballero and Huber* [2013]). The true climate response at high $CO_2$, however, is uncertain: some studies argue that climate system exhibits much greater sensitivity to $CO_2$ in the Eocene [e.g., *Royer et al.*, 2012], or that radiative forcing must have been much higher [e.g., *Huber and Caballero*, 2011]. With regard to the Asian monsoon, some simulations show that the pattern of the monsoon does not change significantly all the way up to 4480 ppmv [*Huber and Goldner*, 2012; M. Huber, personal communication, 2016]. All other factors are held at their modern levels.
3. *Glacial lower boundary conditions.* We evaluate the difference in climate caused by introducing the last glacial maximum (LGM) ice sheets and sea level as a lower boundary condition in the model, based on the ICE-5G reconstruction of *Peltier* [2004]. The lowering of sea level radically rearranges the land-sea distribution in the maritime continent: the exposure of the Sunda shelf connects the major islands of Southeast Asia to each other and to the mainland; and the exposure of the Arafura shelf connects New Guinea to Australia (Figure 2b). Other land surface conditions and atmospheric $CO_2$ are held at the control (i.e., modern) values, and sea ice evolves with ocean surface temperatures.
4. *Displacement of the Indian subcontinent.* We evaluate the difference in climate caused by pulling the Indian subcontinent back approximately 2500 km to the south-southwest (Figure 2c). Our geometry is inspired by plate reconstructions at the time of collision [e.g., *Molnar and Stock*, 2009]. Moreover, ignorance of past topography permits a range from a low surface to a wide, high plateau. In the main experiment reported on here, we retain the modern Himalaya topography at the estimated location of the suture, while elsewhere the elevations are set to zero. Land surface parameters were set at the modern values of an interior point of the India Peninsula. For brevity we will refer to this experiment as "Himalaya South." As extreme end-members, we also performed experiments in which the Himalaya were also flattened ("South Flat," Figure 2e), and in which a high, wide interior plateau was retained ("Mega Tibet," Figure 2f). We will briefly report the results of these.
5. *An inland sea*. Finally, we evaluate the difference in climate caused by introducing a large inland sea to our Himalaya South configuration (Figure 2d). The extent of the sea is loosely inspired by some reconstructions for the Paratethys Sea *Popov et al.* [2004]. In our experiments, land points are replaced with a 50 m deep ocean slab (at sea level) with no *q* fluxes. We refer to this numerical experiment as "Paratethys." Obviously, the actual land-sea distribution was much more complex and varied substantially over time [e.g., *Popov et al.*, 2004]. Our intent is to explore the impact of an inland sea on continent-scale patterns of circulation and precipitation. We cannot capture local climatic effects (on scales of ~100 km), which depend sensitively on local topography and the proximity to water bodies. For example, the modern seasonality of precipitation is completely different inside and outside of the Lake Issyk-Kul basin [e.g., *Romanovsky*, 2002]. Such local variability renders fragile the large-scale interpretation of any hydrologic environmental proxy from such settings. We also performed an experiment with a larger Paratethys Sea extending to the Atlantic ("Big Paratethys," Figure 2g).

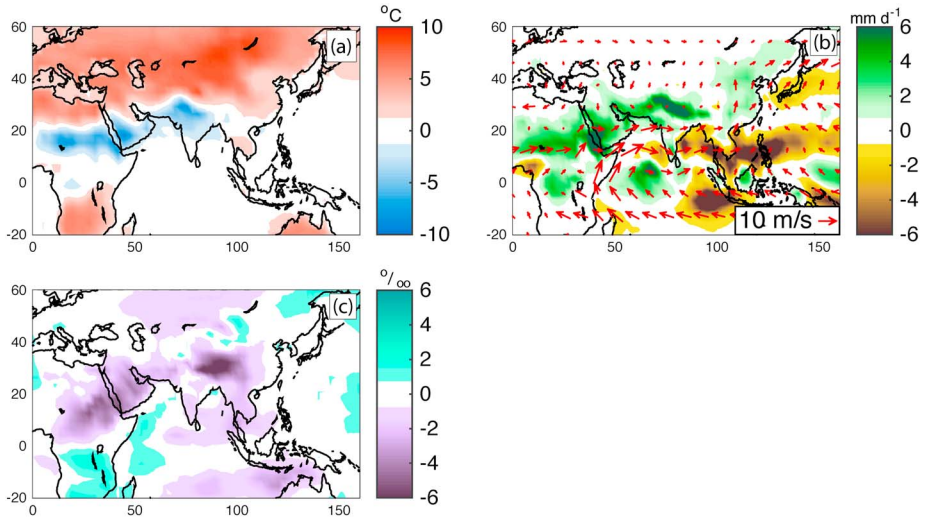


**Figure 3.** Climate differences due to insolation differences between 218 kyr B.P. and 207 kyr B.P.: (a) JJA near-surface air temperatures; (b) JJA precipitation and the 850 mbar winds from the 218 kyr B.P. experiment; (c) annual-mean P-weighted $\delta^{18}O$ (see equation (1)).

The stylized surface boundary conditions shown in Figure 2 are consistent with our approach to deliberately span a broad range of conditions that Asia may have experienced since the Indian-Eurasian plate collision. Of course, the above list of geologic factors affecting Asia's climate is not exhaustive, and other potentially important influences will be discussed later in the paper.

### 3.1. Orbital Configuration

*Battisti et al.* [2014] discussed these two experiments in detail. In response to the higher insolation at 218 kyr B.P. relative to 207 kyr B.P., calculated JJA temperatures increase substantially over the Northern Hemisphere continents, exceeding 8°C in places (Figure 3a). The higher JJA insolation also extends into the Southern Hemisphere, raising continental temperatures (during SH winter) there. The SST differences are muted compared to land temperatures. Because of the thermal inertia of the ocean mixed layer, the seasonal cycle in SST is in quadrature with that of the insolation, and the springtime insolation intensities at 218 kyr B.P. and 207 kyr B.P. are in fact quite similar. Therefore, the summertime SSTs are similar in the two experiments.

The striking exception to the overall land warming is a zone of 3 to 5°C cooling extending across the Sahel, Arabia, and India, for 218 kyr B.P. As demonstrated by *Rupper et al.* [2009] and *Battisti et al.* [2014], enhanced insolation drives a stronger monsoon in these regions, producing both more clouds (that reflect solar radiation back to space) and more evaporation (a surface cooling), both of which lead to lower temperatures (e.g., also *Kutzbach and Otto-Bliesner* [1982], *Rupper et al.* [2009], and *Marzin and Braconnot* [2009]) and indeed, it is consistent with the observed cooling over India after the monsoon onset in the modern seasonal cycle. This cooling is one of the few instances we are aware of where the response of the atmospheric circulation is strong enough to overcome the tendency of the direct radiative forcing.

The stronger monsoon across the Sahel, Arabia, and India, for 218 kyr B.P. is evident in the precipitation field (Figure 3b). Rainfall on the southern flank of the Himalaya for 218 kyr B.P. exceeds that for 207 kyr B.P. by 6 mm $d^{-1}$, and therefore is approximately 50% greater. Over Arabia, the enhancement of about 4 mm $d^{-1}$ is a 400% increase, and the energetics and dynamics of the monsoon are fundamentally reorganized there [*Battisti et al.*, 2014]. For 218 kyr B.P. low-level westerly winds over Africa (Figure 3b) bring much of the water vapor in the Horn of Africa and Arabia from the Atlantic. These winds differ from those of today (Figure 1b) when northerly winds transport little moisture to these regions. The increase of precipitation in the Sahel and Arabia is a direct result of intense solar heating driving local maxima in moist static energy over which deep convection becomes organized (see section 4 and *Battisti et al.* [2014]). Precipitation also increases, but less dramatically, over much of eastern China, due to increases in moist static energy associated with the increase in temperatures (see section 4).

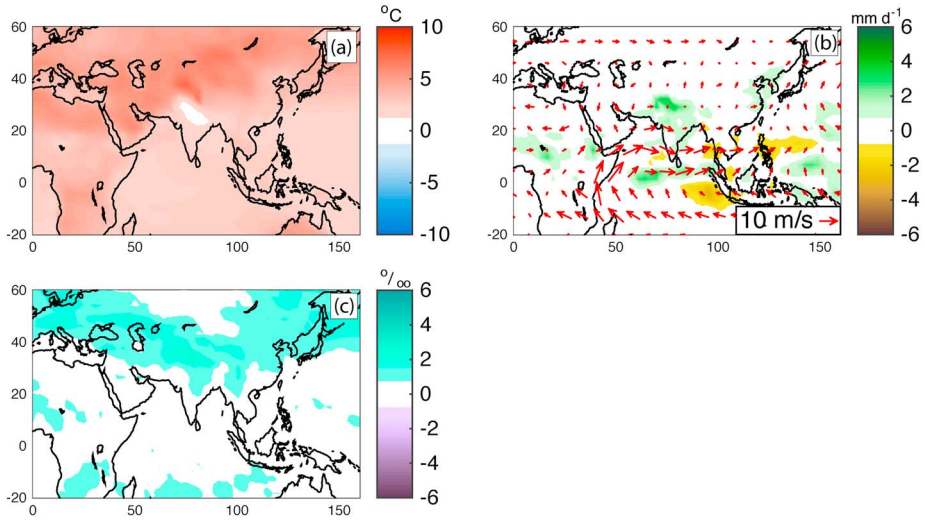


**Figure 4.** Climate differences due to doubling $CO_2$ from 360 ppmv to 720 ppmv. Plotting conventions are as in Figure 3, except that 850 mbar winds in Figure 4b are from the 720 ppmv experiment.

At 218 kyr B.P., the overall pattern of circulation at low levels over the Indian Ocean and southern Asia, reflected in the 850 mbar winds (Figure 3b), is quite similar to the modern (Figure 1b), with a strong cross-equatorial flow in the Somali jet and surface westerlies across much of India. The large reductions in precipitation west of Sumatra and east of Vietnam are colocated with climatological maxima in the ECHAM model (Figure 1d). These precipitation maxima are not seen in observations (Figure 1b), however, and so the model patterns in these regions should not be taken too seriously; they are associated with relatively small differences in the circulation that can nonetheless cause quite large differences in the moisture flux convergence.

$\overline{\delta^{18}O_P}$ is strongly depleted over Tibet (−6‰) and southeast China (−2‰). *Battisti et al.* [2014] demonstrate that this depletion is due to water vapor sourced from the Indian ocean that has experienced enhanced precipitation over the Indian subcontinent. Wherever the surviving vapor subsequently precipitates, it contributes to a depleted $\overline{\delta^{18}O_P}$ signal. Finally, *Battisti et al.* [2014] show that the strong depletion over Arabia is a direct response to stronger local precipitation [*Fleitmann et al.*, 2011].

### 3.2. Atmospheric Carbon Dioxide

A doubling of carbon dioxide from 360 ppmv to 720 ppmv produces a relatively uniform JJA warming of about 2°C over the oceans, increasing to about 5°C over midlatitude continents (Figure 4a). An exception is over India, where a slightly enhanced monsoon (0 to 2 mm $d^{-1}$, Figure 4b) provides a cooling tendency via the same mechanism articulated in the previous subsection. The result is almost no JJA temperature difference.

Generally, gradients in the thermal forcing of the atmosphere cause the largest differences in circulation, and consequently, in the convergence and divergence of the flow. However, the overall pattern of forcing associated with $CO_2$ differences is quite uniform in both space and time. Because of this, the differences in atmospheric circulation and precipitation are relatively small (Figure 4b) and, therefore, the $\overline{\delta^{18}O_P}$ response is also fairly uniform: an enrichment of 1 to 2‰ over land (Figure 4c), consistent with increased specific humidity (not shown) and thus less Rayleigh fractionation over a warmer continent [e.g., *Tindall and Haywood*, 2015].

### 3.3. Glacial Lower Boundary Conditions

Inserting the LGM ice sheets and sea level into the ECHAM model produces a general JJA cooling over the Asian continent that is strongest in northern Europe near the ice sheet margin but relatively muted and patchy elsewhere (Figure 5a) and which, for the most part, is not statistically significant. The absence of a strong response to glacial boundary conditions, in either JJA temperature or precipitation (Figure 5b), reflects basic atmospheric dynamics: the relatively weak summertime midlatitude circulation (compared to wintertime) means that the local radiation balance dominates over advection in setting the climatic response. In essence, summertime Asia does not particularly notice the physical presence of the vast ice sheets over Fenoscandia and North America. Of course it should be emphasized that, as we saw in the previous section, the $CO_2$ effects of an ice age are felt over Asia, particularly in JJA temperature (Figure 4a).

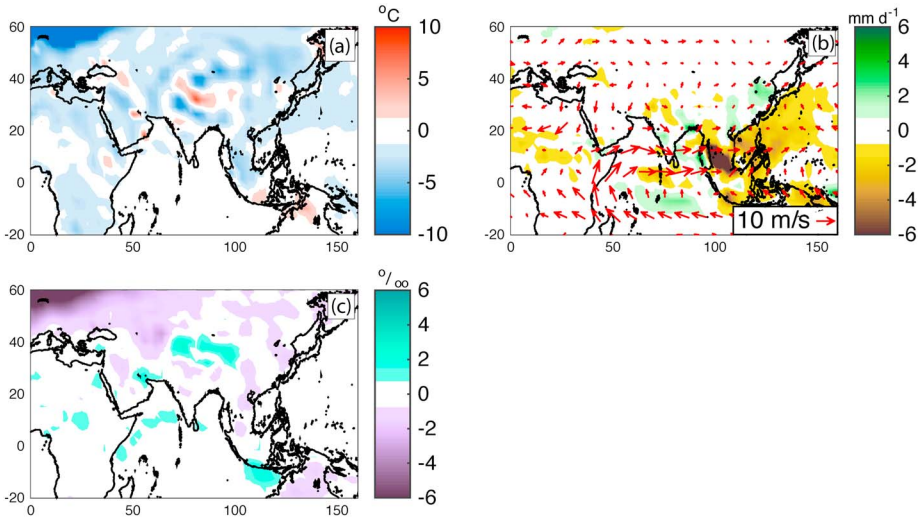


**Figure 5.** Climate differences due to imposing the ice sheets and sea level of the LGM. Plotting conventions are as in Figure 3, except that 850 mbar winds in Figure 5b are from the LGM ice sheet experiment. The coastline is the $z = 0$ contour from the ICE-5G reconstruction [*Peltier*, 2004], which differs from the coastline in the other figures (particularly in southeast Asian and the maritime continent).

Figure 5a also shows that ECHAM simulates a cooling in southeast Asia where land replaces water (cf. Figures 2a and 2b), consistent with a dark ocean being replaced by brighter land. Lowered sea levels also lead to a strong drying (exceeding 5 mm $d^{-1}$ in places) in the region that extends from the Malay peninsula to the island of Borneo (Figure 5b), which demonstrates the acute sensitivity of the pattern of tropical precipitation to small differences in the pattern of surface temperature and circulation. However, the modeled precipitation differences should be interpreted with caution, since they occur near a precipitation maximum in the model climatology that is not seen in the observations (cf. Figures 1b and 1d).

Differences in $\overline{\delta^{18}O_p}$ (Figure 5c) shows a strong depletion over the cold, high ice sheet, but elsewhere differences are small (<2‰) and generally follow differences in regional temperatures, with lower temperatures associated with greater depletion of $^{18}O$.

### 3.4. Displacement of Indian Plate

The Himalaya South experiment possesses several notable features that are expressed best using both its model climatology (Figure 6) and differences from the control experiment (Figure 7). In the figures, both the modern and altered coastlines are contoured. One striking aspect of the Himalaya South climatology is the high summertime temperatures peaking at 45°C (Figure 6a), concomitant with extremely low precipitation (Figure 7b), in the region currently occupied by the Tibetan plateau, central India, and the Bay of Bengal. These fierce desert conditions are more extensive and more intense than any place on Earth in the modern climate (modern Arabia peaks at about 38°C in the summer mean, Australia, and the Sahara peak at about 36°C). Such a climate results from the combination of intense solar heating at subtropical latitudes together with the region's extreme isolation from moisture sources that would otherwise provide the twin buffering effects of

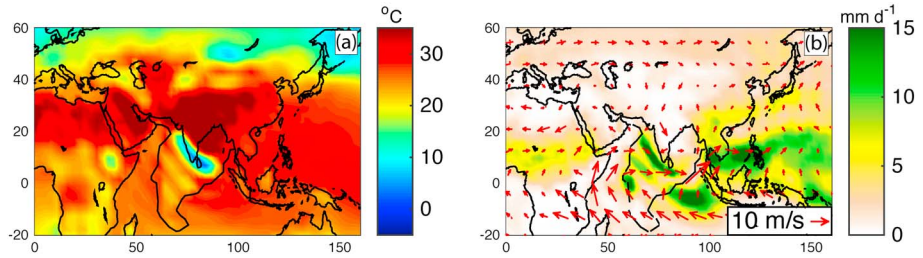


**Figure 6.** Climatology of the Himalaya South experiment: (a) JJA near-surface air temperatures, which peak at 45°C in the regions from which the Tibetan plateau has been removed; (b) JJA precipitation, and 850 mbar wind vectors.

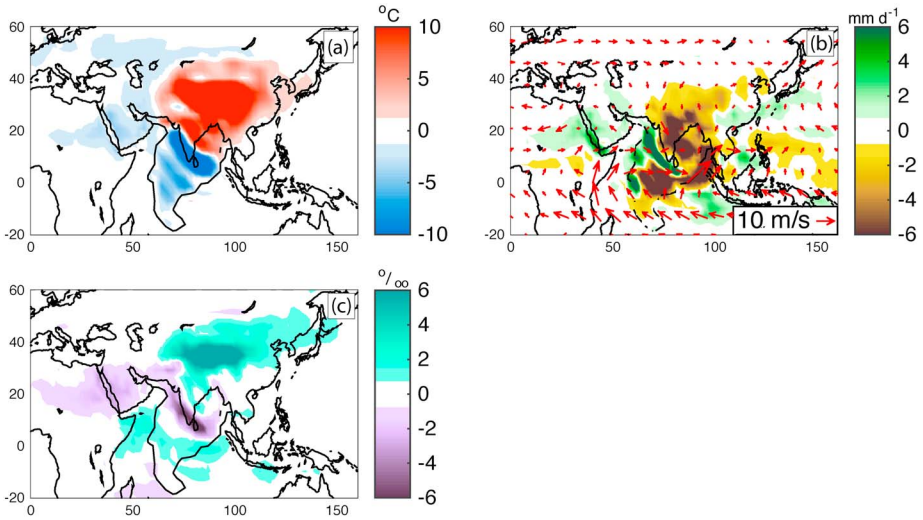


**Figure 7.** Climate differences between the Himalaya South experiment and the control experiment. Plotting conventions are as in Figure 3, except that 850 mbar winds in Figure 7b are from the Himalaya South experiment.

reflective clouds and surface evaporation [e.g., *Rupper et al.*, 2009]. In the next section we show that the presence of a Paratethys Sea acts to ameliorate these extreme conditions. The climate of the southward displaced Himalayas is also characterized by cool JJA temperatures at elevation and an upwind orographic precipitation peak (Figures 6a and 6b). To the southwest of the displaced Himalayas a weak double-band pattern can be seen in the fields shown in Figures 6a, 6b, 7a, and 7b. This is a Gibbs phenomenon—a few hundred meters of topography exists as an artifact of the spectral truncation of the sharp topographic front introduced into the GCM [e.g., *Holzer*, 1996], and therefore, these precipitation bands should be ignored. Although there are clearly big differences in local climate and strong orographic influences, the overall structure of the continental-scale circulation remains recognizably monsoonal, with a cross-equatorial low-level circulation in the Arabian Sea, convergence and precipitation over Southeast Asia, and upper level divergence (albeit with a center shifted to the east, section 4). Our results are consistent with recent studies simulating more realistic Eocene conditions and new paleoclimate data [*Huber and Goldner*, 2012; *Licht et al.*, 2014] and which find a modern-like Asian monsoon back to 40 Ma.

Turning to the difference plots, the largest differences in JJA near-surface temperatures (Figure 7a) can be clearly linked to elevation, with higher temperatures over lowered terrain, and the inverse; and to land-sea distribution where a higher land albedo leads to cooling over the displaced Indian continent. In this latter case, a warming might be expected, given the lower heat capacity of the land compared to the ocean it replaces. The displaced continent, however, straddles the equator, where the seasonality of insolation is weak.

Precipitation for the Himalaya South experiment (Figure 7b) has several modes of response: precipitation is reduced where the displaced Indian continent replaces ocean. Replacing ocean with land reduces moisture, temperature, and low-level moist static energy (Figures 9b and 9f); precipitation is increased where westerlies impinge on the slopes of the displaced Himalayas; and precipitation is strongly reduced in the lee of the displaced Himalayas and throughout the region of modern India and Tibet. The effect of the isolation of the continental interior from moisture sources on precipitation trumps the effects of lower surface elevations and warmer temperatures.

Over regions where the modern Tibetan plateau was removed, $\overline{\delta^{18}O_P}$ is enriched because the vapor from which precipitation forms is less depleted once the orography is removed (Figure 7c). $\overline{\delta^{18}O_P}$ is strongly depleted over the highest elevations of the displaced Himalaya because $^{18}O$ has continually been removed by condensation of water vapor that then falls as intense precipitation on the steep slopes to the southwest Finally, enhanced precipitation and the amount effect lead to a negative $\overline{\delta^{18}O_P}$ signal over Arabia.

It is remarkable that despite such a large rearrangement of the continental geometry, climate impacts are small outside of the regions of the current Tibetan Plateau and of the displaced Indian continent. The most prominent is a slightly cooler, rainier, and more $\overline{\delta^{18}O_P}$ depleted Arabia (Figures 7a–7c), associated with modest circulation differences (Figure 7b). Overall, however, the climate differences are localized to places where the

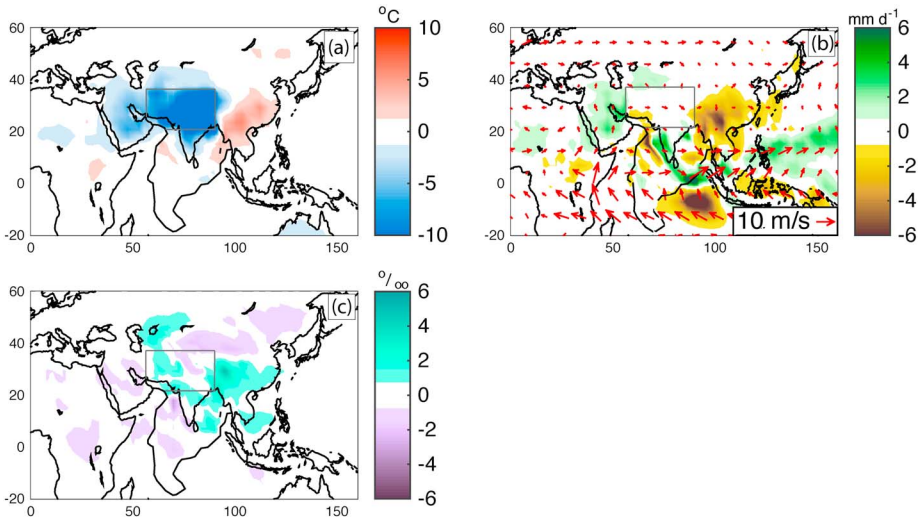


**Figure 8.** Climate differences between the Paratethys experiment and the Himalaya South experiment. Plotting conventions are as in Figure 3, except that 850 mbar winds in Figure 8b are from the Paratethys experiment. The extent of the idealized Paratethys is indicated by the grey box.

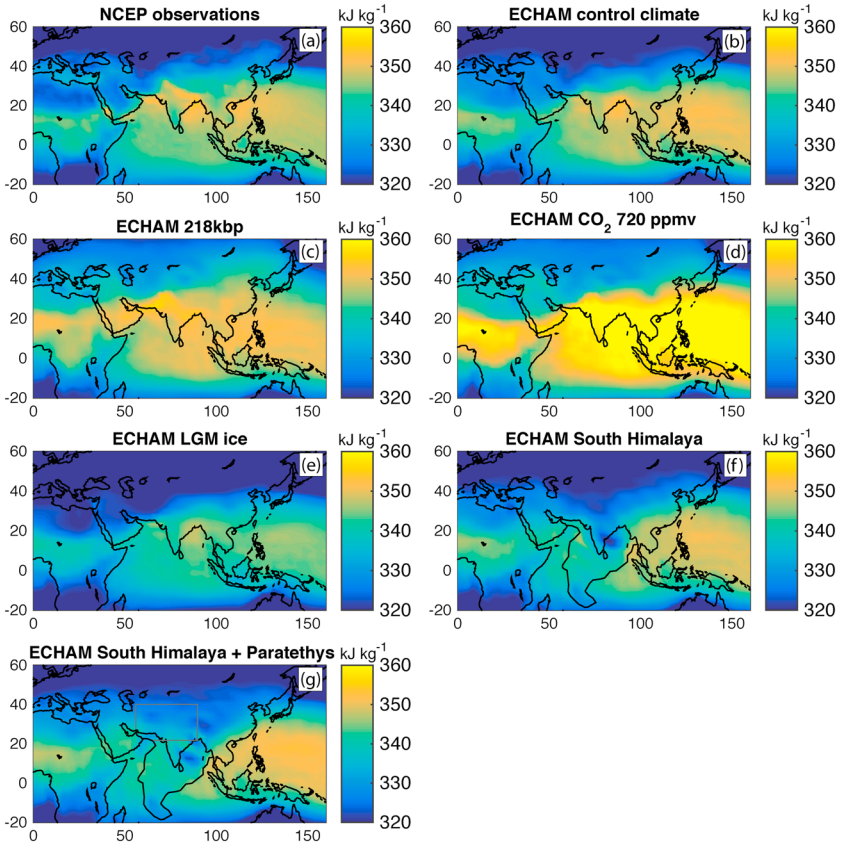


**Figure 9.** (a) Observed JJA moist static energy from NCEP reanalysis, *h*, at 20 mbar above the surface. Remaining panels are the same field, taken from our ECHAM model experiments: (b) control; (c) 218 BP insolation; (d) LGM ice sheets and sea level; (e) 720 ppmv $CO_2$; (f) South Himalaya; and (g) South Himalaya plus Paratethys.

topography was changed, and the results reinforce the dominance of radiation over atmospheric dynamics in summertime climates. We found this also to be the case for the near-surface climate fields for both the Flat South and Mega-Tibet experiments (Figure 2e and 2f).

### 3.5. An Inland Sea

Finally, we consider the influence of adding an idealized Paratethys Sea into what is otherwise the same land-sea geometry and topography of the Himalaya South experiment. The most obvious and dramatic impact of the sea is a strong local summertime cooling of about 8°C (Figure 8a) over and adjacent to the sea. This is simply the moderation of the local seasonal cycle due to the imposed water body (both its thermal inertia and evaporation). The cooling is largest toward the continental interior, where the seasonal cycle is largest. The cooling acts as a low-level thermal forcing that generates anomalous high pressure, and hence an anticyclonic circulation over the cooling (not shown, see, e.g., *Hoskins and Karoly* [1981]). The effect of this circulation is to extend the cooling westward to Arabia, where moderating southerly winds bring lower maritime temperatures and enhanced moisture fluxes lead to higher precipitation (Figures 8a and 8b).

Contrary to our expectations, introducing this vast water source into central Asia did virtually nothing to the local precipitation (Figure 8b). The reduced temperatures generate a stable lower atmospheric boundary layer that keeps low-level moist static energy levels low (see section 4 and Figure 9f), which in turn inhibits deep convection. In this regard, the model Paratethys simply operates as a much larger version of the modern Caspian and Aral Seas. In the modern climate these water bodies are not regions of enhanced summertime precipitation (e.g., Figure 1b).

The Paratethys experiment includes a strong reduction in precipitation of several mm $d^{-1}$ over the region to its east, southeast China. The Paratethys anticyclone is collocated with low-level divergence (because of surface friction, e.g., *Hoskins and Karoly* [1981]). This opposes what would otherwise be low-level convergence over the continent, and so generally weakens summer rainfall. The reduced cloudiness and evaporative cooling leads to a warming over southeast China. Along with this reduced precipitation there is an enrichment of about 2‰ in the $\overline{\delta^{18}O_p}$ in southeast China.

Finally, we also conducted an experiment with a larger Paratethys Sea extending to the Atlantic (Figure 2g). For climate over Asia, this did not introduce any noteworthy differences from our standard Paratethys experiment.

## 4. A Modern Perspective on Monsoon Dynamics

Over the last 20 years, a series of studies has formulated a new perspective on monsoon dynamics that is rooted in the partitioning of the various terms in the energy budget. In essence, the deep convection that characterizes regions of heavy monsoonal precipitation tends to organize over regions where the *moist static energy* maximizes in the subcloud atmospheric boundary layer [*Emanuel et al.*, 1994]. Upper tropospheric temperature maxima reflect locations of deep convective heating [*Privé and Plumb*, 2007a], which are (in the deep tropics at least) dynamically balanced with upper level mass-flux divergence [e.g., *Hoskins and Karoly*, 1981].

This quasi-equilibrium perspective is not a prognostic theory—it does not describe how that balance arises in the first place—but it is a powerful diagnostic constraint in observations and models. Quantifying the characteristic magnitude of the terms involved can help motivate this perspective. Moist static energy is defined as

$$h = c_p T + Lq + gz, \tag{2}$$

where $c_pT$ is the sensible heat per unit mass (the product of heat capacity at constant pressure, $c_p$, and temperature, $T$); $L_vq$ is the latent heat per unit mass (the product of latent heat of vaporization specific humidity, $q$); and $gz$ is the potential energy per unit mass (the product of gravity, $g$, and the height, $z$, of the parcel). Since kinetic energy can be neglected, they comprise the total energy content of said parcel. The timescales for radiative damping (weeks), and large-scale flow (days) are long compared to that for deep convection (hours), and so convecting air masses approximately conserve their total energy. In round numbers, an air parcel acquires approximately $1.5 \times 10^5$ J $kg^{-1}$ of potential energy in ascending from the surface to the tropical tropopause at $z \simeq 15$ km. This energy comes in an approximately 2:1 ratio from the sensible heat release due to an adiabatic cooling of about 100 K ($1 \times 10^5$ J $kg^{-1}$), and the latent heat release due to the condensation of a characteristic tropical specific humidity of 20 g $kg^{-1}$ that such a cooling must entail ($0.5 \times 10^5$ J $kg^{-1}$).

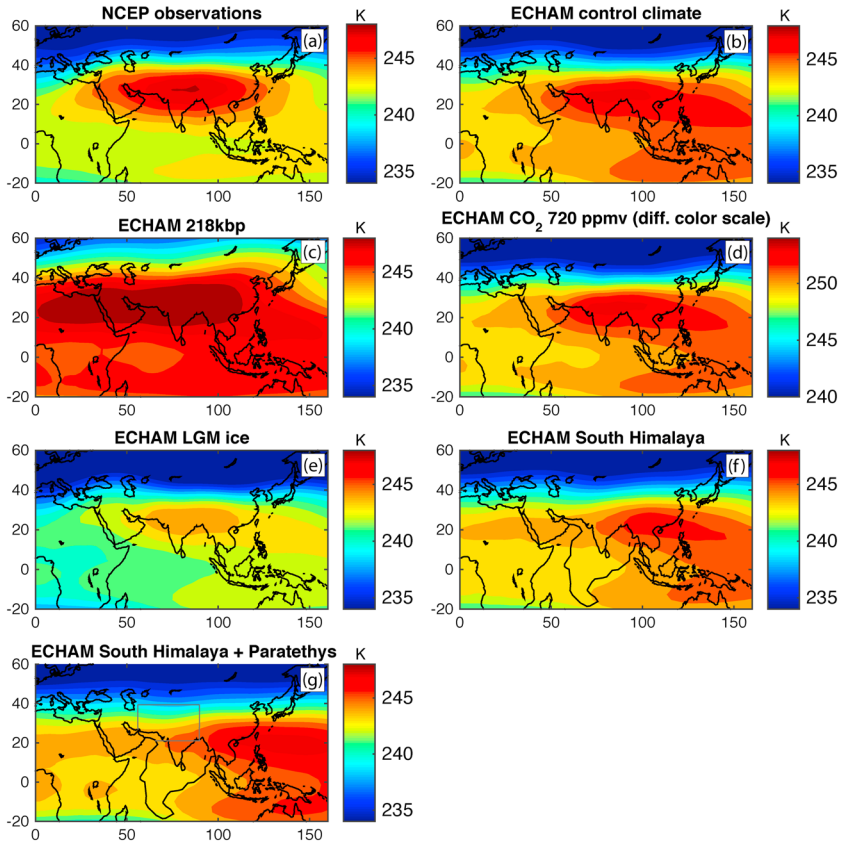


**Figure 10.** (a) Observed JJA upper tropospheric temperature from NCEP reanalysis, averaged from 450 mbar to 250 mbar. Remaining panels are the same field, taken from our ECHAM model experiments: (b) control; (c) 218 kyr B.P. insolation; (d) LGM ice sheets and sea level; (e) 720 ppmv $CO_2$; (f) South Himalaya; and (g) South Himalaya plus Paratethys.

The Clausius-Clapeyron relation dictates an exponential dependence of specific humidity on temperature [e.g., *Holton and Hakim*, 2013]. This means that moisture availability plays a dominant role in setting the location of $h$ maxima near the surface: at $T \sim 30°C$, typical of the tropics, and assuming 80% relative humidity, a 1°C increase provides an additional 1000 J kg$^{-1}$ of sensible heat but an extra 3000 J kg$^{-1}$ of latent heat. From equation (2), with $z = 0$, it is the sum of $c_pT$ and $Lq$ that sets near-surface $h$ and the patterns of convection. Thus, while Arabia may reach almost 40°C in summer, the perennial lack of moisture keeps $h$ low and precludes deep convection in the modern climate. Thus, also, at the onset of the Indian monsoon, $h$ maximizes over the Indian Ocean despite higher temperatures over land. The $h$ maximum moves inland only when the encroaching precipitation increases soil moisture, evaporation, and low-level humidity, even while temperatures over the continent do not change or even fall.

The dominance of $q$ in $h$ is one reason why the old-fashioned view of the monsoon being driven by direct sensible heating from the land is untenable. Another important reason is clearly expressed by *Boos and Kuang* [2013]: a sensible heat pump view of the monsoon requires a reinforcing feedback between precipitation and low-level convergence. However, the convection that brings the precipitation occurs in regions of maximum low-level $h$; low-level convergence into that region will be up the $h$ gradient and so can only ever act to weaken the $h$ maximum.

Figures 9 and 10 display our results in terms of two variables: near-surface $h$ (Note that some monsoon studies present a low-level atmospheric field of equivalent potential temperature [e.g., *Boos and Kuang*, 2010] or moist entropy [e.g., *Molnar et al.*, 2010], each of which have some respective advantages and intepretations. However, the spatial patterns of all these low-level fields are similar.), and upper troposphere temperature averaged between 200 and 450 mbars ($\equiv T_{trop}$) which reflects regions of deep atmospheric heating (i.e., deep convection) and upper level divergence. The ECHAM model captures the spatial pattern of $h$ in the

modern climate (cf. Figures 9a and 9b), although it slightly underestimates the maximum values along the Himalayan front. In terms of $T_{trop}$, the ECHAM control experiment maximum is slightly warmer than observations (≈1°C, cf. Figures 10a and 10b) as represented in National Centers for Environmental Prediction (NCEP) reanalysis (see *Boos and Kuang* [2010] for satellite observations), but with a similar spatial structure. Note that $T_{trop}$ overlies the maximum in $h$, reflecting the tight coupling between them [e.g., *Privé and Plumb*, 2007a, 2007b].

For our climate experiment with the insolation of 218 kyr B.P., $h$ increases across Asia compared to the control (cf. Figures 9b and 9c). Observe that $h$ increases all along the Himalayan front, Arabia, and Saharan Africa, even though temperatures there are cooler (Figure 3a). This is consistent with more moisture and an enhanced monsoon with more clouds and evaporation (Figure 3b). Over Arabia and Saharan Africa, this $h$ maximum is sufficient to initiate deep convection (i.e., monsoon-like precipitation) and is reflected in the upper tropospheric temperature maximum that extends across this region (Figure 10c).

When $CO_2$ is increased to 720 ppmv, $h$ and $T_{trop}$ both increase compared to the control (cf. Figures 9b, 9d, 10b, and 10d—note the change in color scale), but the overall patterns of both fields remain similar. With only small differences in gradients, differences in monsoon circulation and precipitation seen in Figure 4 remain muted. An equivalent result applies for the experiment with LGM ice sheets imposed (cf. Figures 9b, 9e 10b, and 10e): although the values of $h$ and $T_{trop}$ decrease overall, the patterns remain similar to the control experiment, resulting in only small differences to the monsoon.

When the geometry of South Himalaya is introduced, there is significant cooling over what is now the Indian Ocean (Figure 6a) and drying over both the modern Indian Ocean and subcontinent (Figure 6b). This drier continental air means a widespread reduction of $h$ in these regions (also *Boos and Kuang* [2010]). For the South Himalaya experiment, the absolute maximum in $h$ lies over southeast China and the South China Sea (Figure 9f). This is where the greatest concentration of deep convection occurs, as also reflected in the upper level $T_{trop}$ (Figure 10f). It is notable that even with deep heating and upper level divergence displaced far to the east, the basic cross-equatorial inflow at low levels still occurs in the western Indian Ocean (Figure 6b). The South Himalaya experiment also again highlights the crucial role of moisture in setting the pattern of $h$. Over regions where the modern Tibetan plateau was removed, the searing JJA temperatures that reach 45°C (Figure 6), barely register in the overall pattern of $h$.

Finally, when our idealized Paratethys Sea is added to the South Himalaya geometry, the differences in $h$ are quite small (Figure 9f). The cooler temperatures over the inland sea (Figure 8b) are partially compensated by the increased humidity (without leading to precipitation), which is also advected to the east. The value of $h$ decreases over southeastern China (even though temperature increases there, Figure 8a). This is consistent with the weaker monsoon on land and the region of deep convection being displaced farther offshore (Figure 10g).

## 5. Summary and Discussion

We have imposed large changes in the geometry and forcing of Asia's climate. Perhaps the most striking result is that, at the continental scale, the basic pattern of monsoon circulation remains essentially robust across all the experiments. Low-level, cross-equatorial transport occurs across the Indian Ocean but predominantly in a focussed jet east of Africa [e.g., *Rodwell and Hoskins*, 1995]; ascent of air occurs colocated with regions of deep convection and, at upper levels, outflow occurs from regions of upper level temperature maxima.

To summarize the robustness of the monsoon circulation in our various experiments, we show, in Figure 11, seasonal cycles of *Webster and Yang* [1992] monsoon index: the difference between the zonal winds at 850 mbars and 250 mbars, averaged over 40° to 110°E, 0° to 20°N. The Webster-Yang index is a widely used, large-scale metric that combines monsoonal circulation at lower and upper levels. Overall, ECHAM shows a slight bias compared to the observations, but the amplitude and phasing of the index remain similar for all experiments. Differences are largest between extreme orbital differences in winter (218 kyr B.P.); and for the Himalaya South plus Paratethys experiment in summer. Thus, the results in Figure 11, as well as those in Figures 9 and 10, show that the continental-scale summer circulation in the various experiments differ only in degree and do not reflect fundamentally different dynamics.

At regional scales, on the other hand, there can be a large climate response. Differences in land distribution, elevation, and gradient have strong and easily understandable effects on the following: summertime temperature, via lapse rates and continentality; summertime precipitation, via continentality and orographic

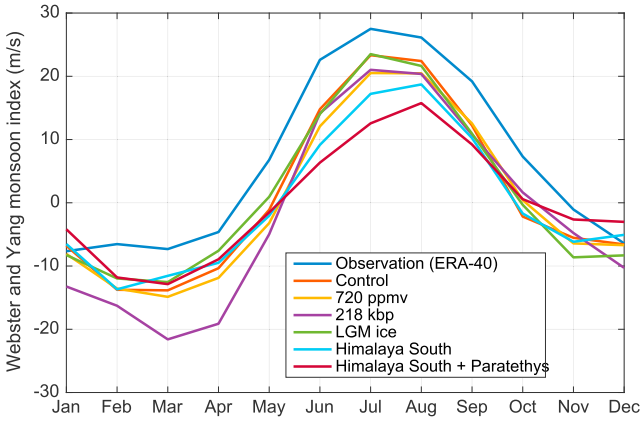


**Figure 11.** The seasonal cycle of the Webster-Yang monsoon index [*Webster and Yang*, 1992], which is the difference between the zonal winds at 850 mbar and at 250 mbar, averaged over a box in the northern Indian Ocean (40° to 110°E, 0° to 20°N); for observations and the six model experiments. Observations are calculated from the ERA Interim [*Dee et al.*, 2011].

precipitation; and $\overline{\delta^{18}O_P}$, via temperature effects, atmospheric advection, and continentality. It was surprising to us that there is so little impact of an inland sea on continental precipitation, and the result might possibly be sensitive to the boundary layer and convection schemes used in our particular climate model. However, the modern Black and Caspian Seas (relics of the Oligocene Paratethys) are observed to have predominantly a local climatic influence. This can be thought of as somewhat akin to the climatological lake effect snowbelts downwind of the Great Lakes in the United States [e.g., *Scott and Huff*, 1996], although the advection of moisture is much weaker in summertime Asian midlatitudes.

A general feature of the experiments in which we imposed geometric changes is that the climate response is largely confined to the regions where geometry is altered, with relatively minor far-field effects (consider the result for LGM ice sheets, for example). Possibly, land surface and vegetative feedbacks, which are not included in our runs, would be capable of expanding the climate response, but our results are consistent with the modern summertime climate where local radiation dominates over advection because of the relatively weak summertime circulation in midlatitudes, compared to wintertime.

Of the experiments in which we imposed changes in climate forcing, the insolation variations associated with different orbital parameters has the largest impact. This must be the case since the magnitude of the forcing (>70 W $m^{-2}$ in the summertime average) is the largest. Such a forcing is large enough to completely reengineer the monsoon dynamics over Arabia and the Sahel, turning torrid desert zones into a torrential monsoonal zones with precipitation rates comparable to much of modern India (Figures 1b and 3b).

Our approach has been to perform idealized climate model integrations rather than attempt simulations of specific time slices. So we have not attempted to evaluate the results against proxy-based reconstructions. However these integrations may be useful to inspire new interpretations and target new work. For example, extensive paleobotanical records from East Asia suggest that central, southern, and eastern China were more arid throughout the Paleocene and Eocene Epochs than today [e.g., *Sun and Wang*, 2005].

In our experiments the largest reductions in precipitation below modern across this region comes from the extra continentality provided by the southward displaced India and, somewhat counterintuitively, by the addition of an inland sea. These two factors combine to reduce summertime precipitation by about 30% compared to the modern (Figures 1b, 7b, and 8b). We have analyzed only summertime precipitation and not other contributions to aridity, such as soil moisture and evaporation. Despite these caveats, we note that a southward displaced India, a narrow Himalayan range, and an inland seaway may satisfy the conditions required for the observed enhanced aridity band across central, eastern, and southern China in the early Cenozoic prior to and just after India-Asia collision.

An important point to emphasize is that there are several examples in our experiments where the old-fashioned view that increased sensible heating from land should drive a more intense monsoon circulation is violated; we see enhanced monsoon and higher moist static energy despite colder surface

temperatures. The interpretation of our results borrows from a now substantial number of studies that view the monsoon through a *quasiequilibrium* balance of terms in the moist static energy budget, studies that span fundamental theory, simplified numerical experiments, comprehensive GCMs, and observations [e.g., *Emanuel et al.*, 1994; *Chakraborty et al.*, 2006; *Privé and Plumb*, 2007a, 2007b; *Bordoni and Schneider*, 2008; *Boos and Kuang*, 2010; *Nie et al.*, 2010; *Boos and Hurley*, 2013; *Merlis et al.*, 2013; *Ma et al.*, 2014; *Walker et al.*, 2015].

The spatial resolution of our climate model does not allow us to evaluate the impact on local climates ($\mathcal{O}$(100 km)), except to indicate the regional-scale tendency. Local topography, water bodies, and vegetation effects can readily cause large local departures from the regional tendency. Resolution at the 100 km scale will always remain an issue in generalizing paleo-environmental reconstructions from individual data sites.

If we compare the patterns of differences across all the experiments (i.e., Figures 3a, 4a, 5a, 7a, and 8a for JJA temperature; Figures 3b, 4b, 5b, 7b, and 8b for JJA precipitation; and Figures 3c, 4c, 5c, 7c, and 8c for $\equiv\overline{\delta^{18}O_p}$), we see some general results. If the climate forcing is quite uniform such as for $CO_2$ and for LGM ice sheets, the pattern of differences is also uniform because gradients of forcing have not changed much (precipitation can be an exception because small difference in the position or intensity of localized precipitation maxima show up as large anomalies). On the other hand, differences in insolation affect seasonality and result in strong differences in land-sea gradients of low-level moist static energy. Geometric differences, too, strongly affect the horizontal and vertical gradients of surface climate.

Overall, the various geologic factors we have considered carry different spatial patterns of climate response. On the one hand, this is a potentially positive outcome in that, by studying patterns of paleo-environmental conditions, it might be easier to make a unique attribution of a given climatic cause. On the other hand, it is a potential negative in that, it increases the possibility of "sample bias," since the state of all of these factors at any given time is highly uncertain. For example, the geologic materials used to make a paleo-environmental reconstruction may subsample one small phase of an orbital cycle, or glacial state, or perhaps be from a period in which continental hydrology was changing rapidly compared to the timescale of interest. For that matter, since we exist now only at one instant within an orbital cycle, one must be careful about climate model experiments in which the differences from the modern climate are interpreted as (for instance) "the impact of changing topography on Asian climate": our modern climate is as much a consequence of our current orbital configuration as it is of our current continental distribution.

As noted in section 1, we have not considered all the geologic factors that have changed over the last 50 Ma, such as the onset of Antarctic and Greenlandic glaciation, abrupt changes in sea ice extent during glaciations, the opening of the Drake Passage, the desiccation of the Mediterranean during the Messinian, and significant evolution of major biomes, have all taken place. With the possible exception of biome changes, which have the potential for significant but poorly understood feedbacks on surface albedo and evapotranspiration, we feel it is unlikely that any of these factors would have as large an impact as those we have considered: we have repeatedly seen a predominantly local response of summertime climate to local differences in forcing. Of the climate fields we have considered, it is likely that $\overline{\delta^{18}O_p}$ is the most mutable, since previous studies have shown it is sensitive to small differences in the relative mixture of evaporative sources and to transport pathways [*Pausata et al.*, 2011; *Battisti et al.*, 2014].

Finally, although we have made some radical changes to the forcing of Asia's summertime climate (as large as any that can be plausibly entertained in the last 50 Ma), we find that the modeled climate differences are, for the most part, not particularly surprising. In this context is noteworthy that, until a few years ago, the prevailing view was that the Asian monsoon was a geologically recent feature (8 to 10 Ma, e.g., *Prell and Kutzbach* [1992]; see *Molnar et al.* [2010] for a review). Our results suggest otherwise and are consistent with other recent studies: using fully coupled comprehensive climate simulations and paleoclimate data, *Huber and Goldner* [2012] and *Licht et al.* [2014] conclude that a modern-like Asian monsoon was present at least as far back as 40 Ma; and also with *Boos and Storelvmo* [2016], who find no abrupt shifts in monsoon strength for a wide range of radiative forcing.

The general agreement of our experiments with such fully coupled models suggests that our use of fixed $q$ fluxes and a mixed layer, which preclude any representation of ocean circulation changes, does not seriously undermine our results (supporting this, the response of a variety of climate models to differences in orbital precession has been shown to be insensitive to the choice of mixed-layer or dynamic ocean

(X. Liu, et al., Tropical precipitation and cross-equatorial ocean heat transport during the mid-Holocene, *Journal of Climate*, in review, 2016)). Further, we suggest that the recently developed perspective of the Asian monsoon in terms of a quasi-equilibrium moist-static energy balance can be productively applied to interpretations of past monsoons in the geologic record. We have been able to understand the tendencies (though perhaps not the magnitudes) of the climate differences from basic principles of atmospheric science. In this study we deliberately conducted idealized experiments rather than an actual simulation, but we also did perform a few experiments in which we changed multiple factors together (land-ice and insolation, for example). The results are approximately linear; that is, the sum of the response to changing each factor individually is approximately the same as changing them together. Therefore, for an actual simulation of a reconstructed geometry, atmospheric composition, and a particular set of orbital conditions, our results provide some confidence that the effects of all the various changes can be disaggregated and understood.

## Appendix A: Wintertime Patterns

For the sake of completeness we present figures showing a few of the wintertime (December to February, or DJF) climate fields from the various model experiments, largely without comment. We show surface temperature (Figure A1); precipitation and sea level pressure (which must be extrapolated beneath topography, Figure A2); and 500 mbar heights (contours of which shows the midtropospheric jet stream, Figure A3). One feature of note is that sea level pressure anomalies are everywhere positive when LGM ice sheets and sea level are imposed (Figure A2e). This increase in pressure is due to the weight of the air that is displaced by the LGM ice sheets. A simple calculation can provide some insight. Let $R$ be the radius of the Earth, $f_o$ be the fraction of surface area covered by ocean, and $H$ be the LGM sea level fall. The volume, $V$, of air displaced by ice sheets is $V = 4\pi R^2 f_o H$. The increase in sea level pressure is the weight of this air (density $\equiv \rho_o$) divided by the total surface area of the Earth, giving $\Delta p = \rho_o g V / 4\pi R^2 = \rho_o g f_o H$. Taking round numbers of $\rho = 1.2\text{kgm}^{-3}$, $f_o = 0.7$, and $H = 120$ m, gives $\Delta p \simeq 10$ hPa. This is in fair agreement with difference between the global-mean,

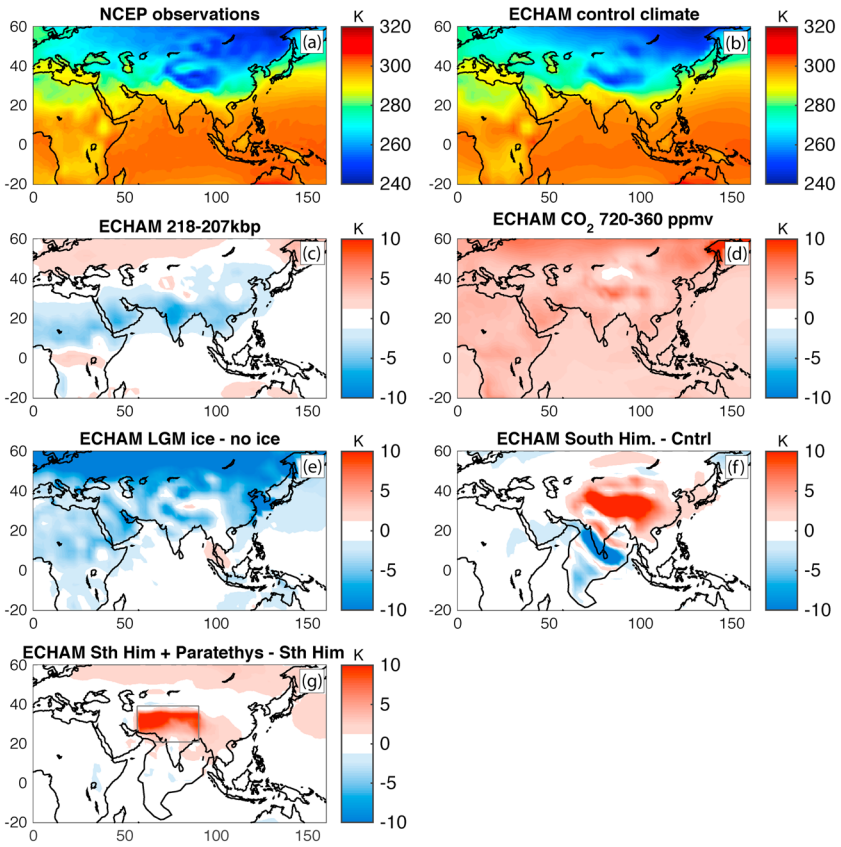


**Figure A1.** DJF surface temperatures from the various model experiments. (a) Observations from NCEP; (b) control simulations; differences between experiments: (c) 218 kyr B.P.–207 kyr B.P.; (d) 720–360 ppmv $CO_2$; (e) LGM ice sheets and sea level minus the control; (f) South Himalaya minus the control; (g) Paratethys Sea minus South Himalaya.

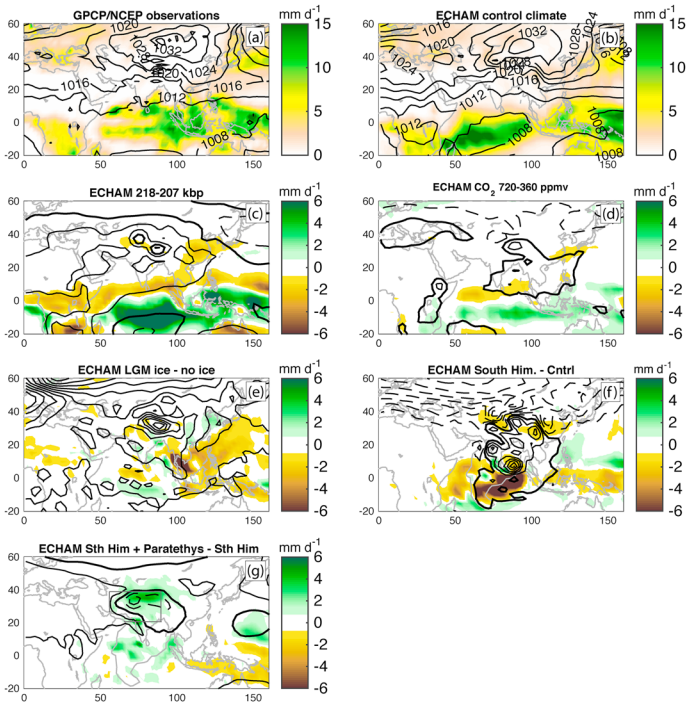


**Figure A2.** DJF precipitation and mean sea level pressure from the various model experiments. As in Figure A1 except that Figures A2a and A2b precipitation climatology from Global Precipitation Climatology product [*Adler et al.*, 2003] contours every 4 mbar; (c)–(g) positive anomalies are shown with solid lines, negative with dashed lines, zero contour is the thick line; contour interval is 2 mbar.

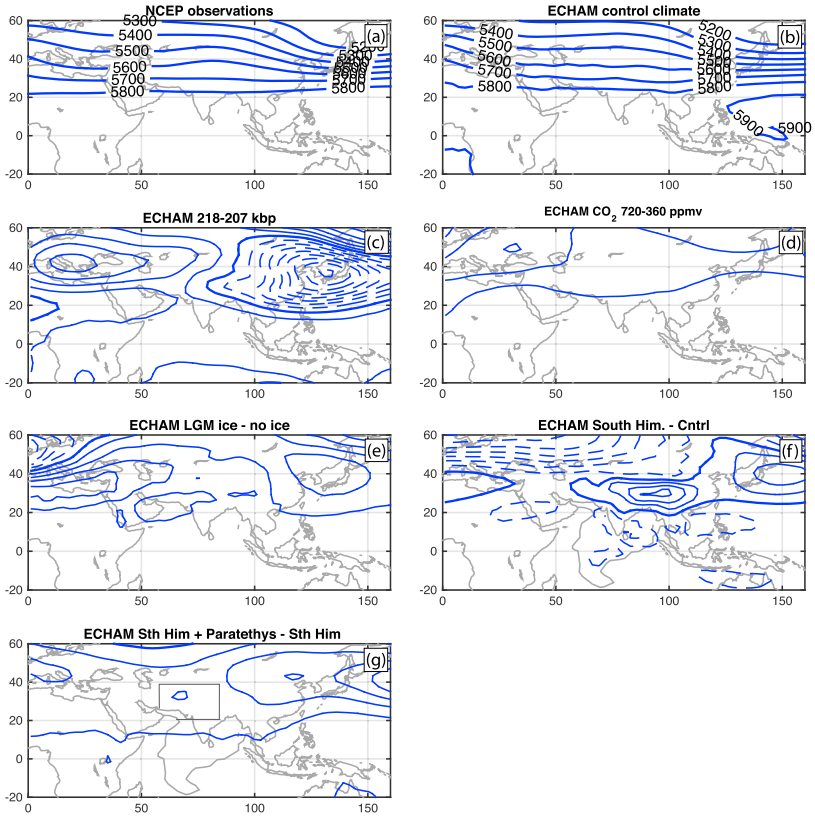


**Figure A3.** DJF 500 mbar heights. As in Figure A1 except that in Figures A3c–A3g positive anomalies are shown with solid lines, negative with dashed lines, zero contour is the thick line, contour interval is 20 m.

annual-mean sea level pressure in the control experiment at 1009.7 hPa and for the LGM boundary conditions at 1021.1 hPa. For the same reason, an average decrease in sea level pressure can be seen in the difference between Himalaya South and control experiments.

There is a striking difference in the DJF 500 mbar height fields in the eastern Pacific for the 218 kyr B.P. minus 207 kyr B.P. insolation experiments. This appears to be a teleconnection pattern due to the strong differences in precipitation in the southern equatorial Indian Ocean (Figure A2c). We have not given this particular result much weight because the ECHAM model DJF climatology in the southern equatorial Indian Ocean is quite different from observations (Figures A2a and A2b).

When the Tethy's sea is included, the DJF temperature increases (Figure A1g) because of the thermal inertia of the water and is associated with a shallow thermal low-pressure circulation (Figure A2g), *Hoskins and Karoly*, 1981).

**Acknowledgments**

We are grateful to M. Huber, T. Merlis, and an anonymous reviewer for detailed suggestions that greatly improved the manuscript, and to R. Leung, the Editor. This work was supported by the National Science Foundation Division of Earth Sciences Continental Dynamics Programs, awards 0908558 and 1210920. Any model output that has been archived will be made freely available upon request to G.H.R. NCEP-NCAR and ERA-interim reanalysis data area, publicly available, were accessed from http://www.esrl.noaa.gov/psd/data/.

## References

Adler, R. F., et al. (2003), The version 2 Global Precipitation Climatology Project (GPCP) monthly precipitation analysis (1979-present), *J. Hydrometeor.*, *4*, 1147–1167.

Battisti, D. S., Q. Ding, and G. H. Roe (2014), A coherent pan-Asian climatic and isotopic response to orbital forcing of tropical insolation, *J. Geophys. Res. Atmos.*, *119*(21), 11,997–12,020, doi:10.1002/2014JD021960.

Boos, W. R., and J. V. Hurley (2013), Thermodynamic bias in the multi-model mean boreal summer monsoon, *J. Clim.*, *26*, 2279–2287.

Boos, W. R., and Z. Kuang (2010), Dominant control of the South Asian monsoon by orographic insulation versus plateau heating, *Nature*, *463*, 218–222.

Boos, W. R., and Z. Kuang (2013), Sensitivity of the South Asian monsoon to elevated and non-elevated heating, *Sci. Rep.*, *3*, 1192, doi:10.1038/srep01192.

Boos, W. R., and T. Storelvmo (2016), Near-linear response of mean monsoon strength to a broad range of radiative forcings, *Proc. Nat. Acad. Sci.*, *113*, 1510–1515, doi:10.1073/pnas.1517.

Bordoni, S., and T. Schneider (2008), Monsoons as eddy-mediated regime transitions of the tropical overturning circulation, *Nat. Geosci.*, *1*, 515–519.

Caballero, R., and M. Huber (2013), State-dependent climate sensitivity in past warm climates and its implications for future climate projections, *Proc. Natl. Acad. Sci.*, *110*, 14162–14167.

Chakraborty, A., R. S. Nanjundiah, and J. Srinivasan (2006), Theoretical aspects of the onset of Indian summer monsoon from perturbed orography simulations in a GCM, *Ann. Geophys.*, *24*, 2075–2089.

Dayem, K., P. Molnar, D. S. Battisti, and G. H. Roe (2010), Lessons learned from the modern monsoon applied to the interpretation of paleoclimate records, *Earth Planet. Sci. Lett.*, *295*, 219–230.

Dee, D. P., et al. (2011), The ERA-Interim reanalysis: Configuration and performance of the data assimilation system, *Q. J. R. Meteorol. Soc.*, *137*, 553–597, doi:10.1002/qj.828.

Emanuel, K. A., J. D. Neelin, and C. S. Bretherton (1994), On large-scale circulations in convecting atmospheres, *Q. J. R. Meteorol. Soc*, *120*, 1111–1143.

Fleitmann, D., S. J. Burns, M. Pekala, A. Mangini, A. Al-Subbary, M. Al-Aowah, J. Kramers, and A. Matter (2011), Holocene and Pleistocene pluvial periods in Yemen, Southern Arabia, *Quat. Sci. Rev.*, *30*, 783–787, doi:10.1016/j.quascirev.2011.01.004.

Hoffmann, G., and M. Heinmann (1997), Water isotope modeling in the Asian monsoon region, *Quat. Int.*, *37*, 115–128.

Hoffmann, G., M. Werner, and M. Heimann (1998), Water isotope module of the ECHAM atmospheric general circulation model: A study on timescales from days to several years, *J. Geophys. Res.*, *103*(D14), 16,871–16,896.

Holton, J. R., and G. J. Hakim (2013), *An Introduction to Dynamic Meteorology*, 5th ed., 532 pp., Academic Press, Amsterdam.

Holzer, M. (1996), Optimal spectral topography and its effect on model climate, *J. Clim.*, *9*, 2443–2463.

Hoskins, B. J., and D. J. Karoly (1981), The steady linear response of a spherical atmosphere to thermal and orographic forcing, *J. Atmos. Sci.*, *38*, 1179–1196.

Huber, M., and R. Caballero (2011), The Eocene equable climate problem revisited, *Clim. Past*, *7*, 603–633, doi:10.5194/cp-7-603-2011.

Huber, M., and A. Goldner (2012), Eocene monsoons, *J. Asian Earth Sci.*, *44*, 3–23, doi:10.1016/j.jseaes.2011.09.014.

Kalnay, E., et al. (1996), The NCEP/NCAR 40-year reanalysis project, *Bull. Am. Meteorol. Soc.*, *77*, 437–470.

Kutzbach, J. E., and B. L. Otto-Bliesner (1982), The sensitivity of the African-Asian monsoonal climate to orbital parameter changes for 9000 Years B.P. In a low-resolution general circulation model, *J. Atmos. Sci.*, *39*, 1177–1188.

Licht, A., et al. (2014), Asian monsoons in a late Eocene greenhouse world, *Nature*, *513*, 501–506.

Ma, D., W. R. Boos, and Z. Kuang (2014), Effects of orography and surface heat fluxes on the South Asian summer monsoon, *J. Clim.*, *27*, 6647–6659.

Marzin, C., and P. Braconnot (2009), Variations of Indian and African monsoons induced by insolation changes at 6 and 9.5 kyr B.P., *Clim. Dyn.*, *33*(2–3), 215–231, doi:10.1007/s00382-009-0538-3.

Masson-Delmotte, V., et al. (2013), Information from Paleoclimate Archives, in *Climate Change 2013: The Physical Science Basis. Contribution of Working Group I to the Fifth Assessment Report of the Intergovernmental Panel on Climate Change*, edited by T. F. Stocker et al., Cambridge Univ. Press, Cambridge, U. K., and New York.

Merlis, T. M., T. Schneider, S. Bordoni, and I. Eisenman (2013), Hadley circulation response to orbital precession. Part II: Subtropical continent, *J. Clim.*, *26*, 754–771, doi:10.1175/JCLI-D-12-00149.1.

Myhre, G., E. J. Highwood, K. P. Shine, and F. Stordal (1998), New estimates of radiative forcing due to well mixed greenhouse gases, *Geophys. Res. Lett.*, *25*, 2715–2718.

Molnar, P., and J. M. Stock (2009), Slowing of India's convergence with Eurasia since 20 Ma and its implications for Tibetan mantle dynamics, *Tectonics*, *28*, TC3001, doi:10.1029/2008TC002271.

Molnar, P., W. R. Boos, and D. S. Battisti (2010), Orographic controls on climate and paleoclimate of Asia: Thermal and mechanical roles for the Tibetan Plateau, *Ann. Rev. Earth Planet. Sci.*, *38*, 77–102, doi:10.1146/annurev-earth-040809-152456.

Nie, J., W. R. Boos, and Z. Kuang (2010), Observational evaluation of a convective quasi-equilibrium view of monsoons, *J. Clim.*, *23*, 4416–4428.

Pagani, M., M. Huber, Z. Liu, S. M. Bohaty, J. Henderiks, W. Sijp, S. Krishnan, and R. M. DeConto (2011), The role of carbon dioxide during the onset of Antarctic glaciation, *Science*, *334*, 1261–1264.

Pausata, F. S. R., D. S. Battisti, K. H. Nisancioglu, and C. M. Bitz (2011), Chinese stalagmite $\delta^{18}O$ controlled by changes in the Indian monsoon during a simulated Heinrich event, *Nat. Geosci.*, *4*(7), 474–480, doi:10.1038/ngeo1169.

Peltier, W. R. (2004), Global glacial isostasy and the surface of the ice-age Earth: The ICE-5G (VM2) model and GRACE, *Ann. Rev. Earth Plan. Sc.*, *32*, 111–149.

Popov, S. V., F. Rögl, A. Y. Rozanov, F. F. Steininger, I. G. Shcherba, and M. Kováč (2004), Lithological-paleogeographic maps of Paratethys, *Cour Forschungsinstitut Senckenberg*, *250*, 1–46.

Prell, W. L., and J. E. Kutzbach (1992), Sensitivity of the Indian monsoon to forcing parameters and implications for its evolution, *Nature*, *360*, 647–652.

Privé, N. C., and R. A. Plumb (2007a), Monsoon dynamics with interactive forcing. Part I: Axisymmetric studies, *J. Atmos. Sci.*, *64*, 1417–30.

Privé, N. C., and R. A. Plumb (2007b), Monsoon dynamics with interactive forcing. Part II: Impact of eddies and asymmetric geometries, *J. Atmos. Sci.*, *64*, 1431–42.

Ramstein, G., F. Fluteau, J. Besse, and S. Joussaume (1997), Effect of orogeny, plate motion and land-sea distribution on Eurasian climate over the past 30 million years, *Nature*, *386*, 788–795.

Rodwell, M. J., and B. J. Hoskins (1995), A model of the Asian summer monsoon, Part II: Cross-equatorial flow and PV behavior, *J. Atmos. Sci*, *52*, 1341–1356.

Roeckner, E., K. Arpe, L. Bengtsson, M. Christoph, M. Claussen, L. Dmenil, M. Esch, M. Giorgetta, U. Schlese, and U. Schulzweida (1996), The atmospheric general circulation model ECHAM-4: Model description and simulation of present-day climate, *Tech. Rep. 218*, 90, Max Planck Institut fur Meteorologie Report Series, Max-Planck-Institut für Meteorologie.

Romanovsky, V. V. (2002), Water level variations and water balance of Lake Issyk-Kul, in *Lake Issyk-Kul: Its Natural Environment*, NATO Science Series, edited by J. Klerkx and B. Imanackunov, pp. 45–59, Kluwer Acad., Netherlands.

Royer, D. L., M. Pagani, and D. J. Beerling (2012), Geobiological constraints on Earth system sensitivity to $CO_2$, *Geobiology*, *10*, 298–310, doi:10.1111/j.1472-4669.2012.00320.x.

Rupper, S. B., G. H. Roe, and A. Gillespie (2009), Spatial patterns of glacier advance and retreat in Central Asia in the Holocene, *Quat. Res.*, *72*, 337–346.

Scott, R. W., and F. A. Huff (1996), Impacts of the great lakes on regional climate conditions, *J. Great Lakes Res.*, *22*, 845–863.

Sperber, K. R., H. Annamalai, I.-S. Kang, A. Kitoh, A. Moise, A. Turner, B. Wang, and T. Zhou (2013), The Asian summer monsoon: An intercomparison of CMIP5 vs. CMIP3 simulations of the late 20th century, *Clim. Dyn.*, *41*, 2711–2744.

Sun, X., and P. Wang (2005), How old is the Asian monsoon system? —Palaeobotanical records from China, *Palaeogeogr. Palaeoclimatol. Palaeoecol.*, *222*, 181–222.

Tindall, J. C., and A. M. Haywood (2015), Modeling oxygen isotopes in the Pliocene: Large-scale features over the land and ocean, *Paleoceanography*, *30*, 1183–1201, doi:10.1002/2014PA002774.

vonStorch, H., and F. W. Zwiers (1999), Statistical analysis in climate research, p. 494.

Walker, J. M., S. Bordoni, and T. Schneider (2015), Interannual variability in the large-scale dynamics of the South Asian summer monsoon, *J. Clim.*, *28*, 3731–3750.

Webster, P. J., and S. Yang (1992), Monsoon and ENSO: Selectively interactive systems, *Q. J. R. Meteorol. Soc.*, *118*, 877–926.

Werner, M., P. M. Langebroek, T. Carlsen, M. Herold, and G. Lohmann (2011), Stable water isotopes in the ECHAM5 general circulation model: Toward high-resolution isotope modeling on a global scale, *J. Geophys. Res.*, *116*, 1–14, doi:10.1029/2011JD015681.

Zhang, YG, M. Pagani, Z Liu, S. M. Bohaty, and R. DeConto (2013), A 40-million-year history of atmospheric $CO_2$, *Philos. Trans. R. Soc. A*, *371*, 20130096, doi:10.1098/rsta.2013.0096.